Geochemistry Geophysics Geosystems G3

*Article*
Volume 13, Number 5
18 May 2012
Q05013, doi:10.1029/2012GC004043
ISSN: 1525-2027

Published by AGU and the Geochemical Society

# Seismic evidence of tectonic control on the depth of water influx into incoming oceanic plates at subduction trenches

**M. Lefeldt**
*SFB 574, Wischhofstrasse 1-3, D-24148 Kiel, Germany*

*GEOMAR, Helmholtz Centre for Ocean Research Kiel, Wischhofstrasse 1-3, D-24148 Kiel, Germany*

*Now at IMS ED, CTBTO, Wagramerstrasse 5, VIC, A-1220 Vienna, Austria (marten.lefeldt@ctbto.org)*

**C. R. Ranero**
*Barcelona Center for Subsurface Imaging, ICREA, Instituto de Ciencias del Mar, CSIC, Pg. Marítim de la Barceloneta 37-49, E-08003 Barcelona, Spain*

**I. Grevemeyer**
*SFB 574, Wischhofstrasse 1-3, D-24148 Kiel, Germany*

*GEOMAR, Helmholtz Centre for Ocean Research Kiel, Wischhofstrasse 1-3, D-24148 Kiel, Germany*

[1] Water transported by slabs into the mantle at subduction zones plays key roles in tectonics, magmatism, fluid and volatiles fluxes, and most likely in the chemical evolution of the Earth's oceans and mantle. Yet, incorporation of water into oceanic plates before subduction is a poorly understood process. Several studies suggest that plates may acquire most water at subduction trenches because the ocean crust and uppermost mantle there are intensely faulted caused by bending and/or slab pull, and display anomalously low seismic velocities. The low velocities are interpreted to arise from a combination of fluid-filled fractures associated to normal faulting and mineral transformation by hydration. Mantle hydration by transformation of nominally dry peridotite to water-rich serpentinite could potentially create the largest fluid reservoir in slabs and is therefore the most relevant for the transport of water in the deep mantle. The depth of fracturing by normal-fault earthquakes is usually not well constrained, but could potentially create deep percolation paths for water that might hydrate up to tens of kilometers into the mantle, restrained only by serpentine stability. Yet, interpretation of deep intraplate mineral alteration remains speculative because active-source seismic experiments have sampled only the uppermost few kilometers of mantle, leaving the depth-extent of anomalous velocities and their relation to faulting unconstrained. Here we use a joint inversion of active-source seismic data, and both local and regional earthquakes to map the three dimensional distribution of anomalous velocities under a seismic network deployed at the trench seafloor. We found that anomalous velocities are restrained to the depth of normal-fault micro-earthquake activity recorded in the network, and are considerably shallower than either the rupture depth of teleseismic, normal-fault earthquakes, or the limit of serpentine stability. Extensional micro-earthquakes indicate that each fault in the region slips every 2–3 months which may facilitate regular water percolation. Deeper, teleseismic earthquakes are comparatively infrequent, and possibly do not cause significant fracturing that remains open long enough to promote alteration detectable with our seismic study. Our results show that the stability field of serpentine does not constrain the depth of potential mantle hydration.

**Components:** 8000 words, 11 figures, 1 table.

**Keywords:** bending; microseismicity; oceanic plates; serpentinization; subduction zone; water influx.

**Index Terms:** 7220 Seismology: Oceanic crust; 7240 Seismology: Subduction zones (1207, 1219, 1240); 8170 Tectonophysics: Subduction zone processes (1031, 3060, 3613, 8413).

**Received** 11 January 2012; **Revised** 19 March 2012; **Accepted** 19 March 2012; **Published** 18 May 2012.

Lefeldt, M., C. R. Ranero, and I. Grevemeyer (2012), Seismic evidence of tectonic control on the depth of water influx into incoming oceanic plates at subduction trenches, *Geochem. Geophys. Geosyst.*, *13*, Q05013, doi:10.1029/2012GC004043.

## 1. Introduction

[2] At subduction zones, incoming oceanic plates bend into the deep sea trench and deform internally by brittle failure in the upper tens of km, depending mainly on plate age. Following *Chapple and Forsyth* [1979] bending of the oceanic lithosphere can be described as the flexure of a thin elastic-perfectly plastic plate, which leads to a tensional regime at the top of the plate, grading into a compressional one at the bottom.

[3] The intraplate earthquakes occurring in the trench-outer rise region are the consequence of stresses due to plate flexure and their interaction with slab pull forces.

[4] This conceptual framework is supported by global compilations of earthquake mechanisms based on waveform inversion, indicating that normal faulting events occur in the uppermost ~25 km of the bending lithosphere and compressional fault behavior dominates at greater depth [e.g., *Seno and Gonzalez*, 1987; *Seno and Yamanaka*, 1996].

[5] This observation is corroborated by the fact that bathymetric surveys of outer rise and trench areas have imaged a pervasively fractured lithosphere [*Masson*, 1991; *Kobayashi et al.*, 1998; *Ranero et al.*, 2003, 2005]. Offshore Nicaragua, faulting and fault growth from the outer rise to the trench axis generate a prominent stairway-like seafloor relief of half grabens (Figure 1). Seismic reflection images of faults indicate that they may cut 10 to 15 km below reflections from the base of the crust into the upper mantle [*Ranero et al.*, 2003].

[6] It has been proposed that such faulting in the trench-outer rise provides a pathway for fluids, which penetrate through the crust into the uppermost mantle and there react with the cold lithospheric material [*Peacock*, 2001; *Ranero et al.*, 2003], changing "water-poor" peridotite to "water-rich" serpentinite [*Peacock*, 2001, 2004] containing up to 13 wt% of chemically bound water. A wealth of subduction zone processes possibly depend on water carried within the slab. For example, dehydration of the slab may trigger intermediate-depths earthquakes [*Raleigh and Paterson*, 1965; *Meade and Jeanloz*, 1991] and melting of the mantle wedge under volcanic arcs [*Rüpke et al.*, 2004].

[7] There is a consensus that water carried in the subducting plate is trapped as free water in porous sediments and void spaces in the igneous crust, and chemically bound in sediment and alteration products in the upper igneous crust [*Staudigel et al.*, 1996; *Jarrad*, 2003]. The role of serpentinite as a volumetrically important transport media of water into the slab has only more recently been proposed [*Ranero et al.*, 2003; *Ranero and Sallares*, 2004]. Evidence for low P wave velocities of the uppermost mantle that may indicate serpentinization comes from seismic wide-angle reflection and refraction data, collected across several subduction trenches [*Ranero and Sallares*, 2004; *Grevemeyer et al.*, 2007; *Ivandic et al.*, 2008; *Contreras-Reyes et al.*, 2007; *van Avendonk et al.*, 2011]. Reduced mantle velocity has been mapped especially in the region of the incoming plate approximately 50 km seawards from the trench axis, where plate bending is strongest. Here, mantle velocities are about 5–7% lower than typical values for the oceanic mantle. Such reduced velocities are best explained by a fractured and altered (serpentinized) mantle. However, due to the mantle velocity structure, active source seismic data have provided information only of the uppermost 3–5 km of the mantle, while bending-related faults and teleseismic earthquakes in the region cut down to greater depths [*Ranero et al.*, 2003; *Lefeldt and Grevemeyer*, 2008].

[8] In this study, we use a joint inversion of active-source seismic data, and both local and regional earthquakes recorded on a network in the trench seafloor to map in three dimensions and for the first time the depth extent of anomalous oceanic mantle velocity. We found that the velocity distribution

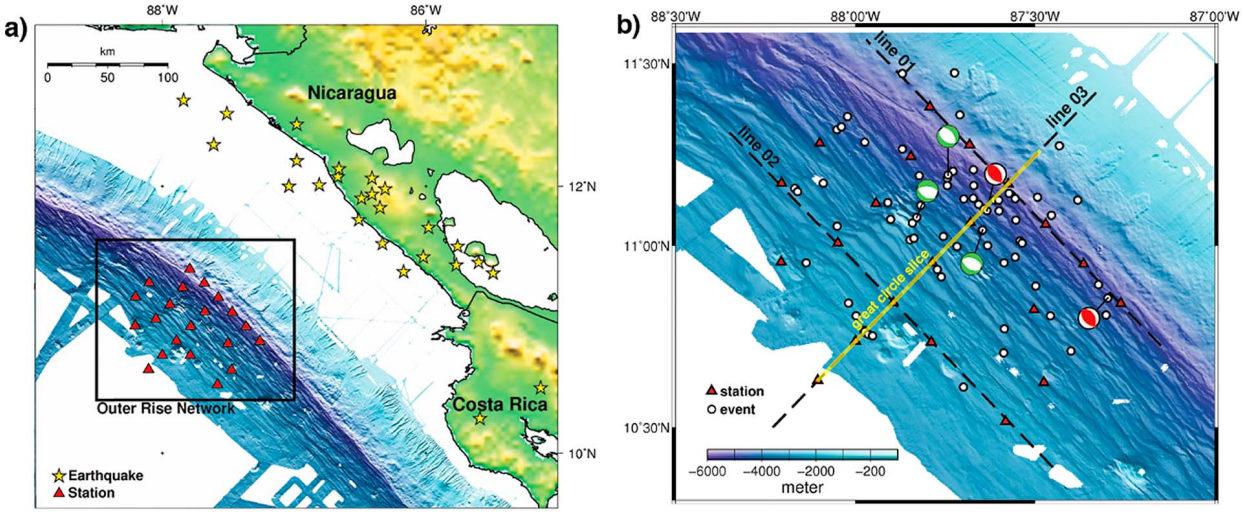


**Figure 1.** Passive seismological and active-source data tracks used in the study. (a) Shaded relief map of Central America and subduction trench. Yellow stars are epicenters of intraslab seismic events [*Syracuse at al.*, 2008] used in the tomographic inversion. Red triangles are stations of the seismological network. (b) Multibeam bathymetry map of the trench. Red triangles are stations of the seismological network, and black dashed lines are active-source seismic profiles. Black circles are micro-earthquake epicenters detected in the network [*Ammon et al.*, 2008]. Focal mechanisms of 3 normal fault (green) and 2 thrust fault (red) events could be determined. The yellow line marks location of great circle cross section in Figure 10a.

indicates that mantle alteration ends shallower than the limit of serpentine stability. Water penetration appears controlled by extensional faulting and fracturing due to bending of the uppermost lithosphere. Micro-earthquakes indicate that large faults slip every 2–3 months due to bending-related stresses. In contrast, normal fault activity during teleseismic earthquakes, although reaching deeper [*Lefeldt and Grevemeyer*, 2008], occurs in a region of normal mantle velocity, which indicates that it does not contribute to significant water influx possibly because it is modulated by interplate coupling and is comparatively infrequent.

## 2. Tectonic Setting

[9] Along the Middle America trench (MAT) subduction rates vary from ∼9 cm/a in the south off Costa Rica to ∼7 cm/a in the north off Mexico, with a slightly oblique subduction (10°) northward of the Central Costa Rica Deformed Belt [*DeMets*, 2001].

[10] Offshore Nicaragua, the age of the plate at the trench axis is roughly 27 Ma [*Barckhausen et al.*, 2001] and multibeam bathymetric mapping of the incoming plate (Figure 1) shows that bending-related faults occur across the ocean trench slope [*Ranero et al.*, 2003]. Heat flow data acquired on the incoming plate support a vigorous water circulation into the ocean plate in area of faulting [*Grevemeyer et al.*, 2005]. Wide-angle seismic data at the Middle America Trench support alteration of the uppermost few km of the oceanic mantle, but do not constrain well the maximum depth that is reached by alteration [*Grevemeyer et al.*, 2007; *Ivandic et al.*, 2010; *van Avendonk et al.*, 2011]. Seismic tomographic images of the slab under Nicaragua support that the subducting upper oceanic mantle is serpentinized [*Syracuse et al.*, 2008]. Additionally, P wave arrivals from intraslab earthquakes at 100–150 km depth show high-frequency late arrivals, which suggest a 2.5–6 km thick low-velocity waveguide at the top of the downgoing plate [*Abers et al.*, 2003] and is best explained by >5 wt% water in the subducted crust, which is 2–3 times higher hydration than inferred for other subduction zones.

## 3. Data, Analysis, and Testing

[11] Data sets used in this study were obtained with a seismic network of ocean bottom seismometers (OBS) deployed in the seafloor of the Nicaragua trench (Figure 1). The network was installed during three months in a region where active seismic experiments had found anomalously low velocities in the uppermost mantle [*Grevemeyer et al.*, 2007; *Ivandic et al.*, 2010].

### 3.1. Data Sets

[12] To constrain the 3D P wave velocity model of crust and upper mantle under the trench, we simultaneously inverted for 3 data sets. These data sets are: (i) active-source wide-angle seismic refraction and reflection data, (ii) local (micro-)earthquakes and (iii) regional earthquakes.

[13] (i) Wide-angle seismic data. Three seismic wide-angle profiles were shot across the network (Figure 1). All OBS recorded all shots of the three profiles, thus providing 3D coverage. In total, 853 Pg-Phases, 653 PmP-Phases and 1198 Pn-Phases travel time picks were used in the inversion.

[14] (ii) Local seismicity. Earthquakes occurring under or in close proximity of the seismological network were used. A description of this data set is given by *Lefeldt et al.* [2009]. A total of 68 local earthquakes with 722 P wave observations were used in the inversion.

[15] (iii) Regional Seismicity. These events occurred in Central America as regional seismicity, located >100 km outside of the seismological network and at depth ranges of 25–160 km (Figure 1). Such events arrive at the receivers at steep angles, after traversing the deep region of the oceanic plate. We used the accurate hypocenter parameters of regional earthquakes from *Syracuse et al.* [2008], which occurred under on- and offshore regions of Nicaragua and Costa Rica during deployment of our network. To perform the 3D-tomographic inversion we selected a subset of 57 events which fulfilled the quality requirements that the first P wave arrival could be picked at least in 10 stations of our network with an accuracy of <100 ms.

[16] Additionally, we evaluated approximately 230 regional events with magnitudes of Mw = 4.6 to 6.0 located under Central America mainland, recorded by the permanent onshore network of the Instituto Nicaragüense de Estudios Territoriales (INETER). Offshore events recorded by INETER were not used due to the large gap in the azimuthal distribution of stations. Comparison of hypocenter parameters of *Syracuse et al.* [2008] and INETER data sets indicates a good agreement. A subset of 17 events from the INETER catalog, giving 513 P wave arrivals, was included in the inversion data sets.

### 3.2. The 3D-Tomography

[17] We used the Fortran 90 software package FMTOMO [*Rawlinson and Urvoy*, 2006; *Rawlinson et al.*, 2006]. In FMTOMO, velocity is represented by a regular grid of points, interpolated by cubic B-splines to define a continuum. The grid has 12 equal spaced points in north–south and in east–west direction (about 7 × 7 km spacing). Each grid cell is refined by a factor of 7 in both, longitudinal and latitudinal direction if a source is present within this particular cell. Focal depths for all local sources calculated with a minimum 1D-velocity model show a range of 0.0 km to 17.4 km beneath seafloor, respectively 4.9 km to 22.7 km beneath sea level [*Lefeldt et al.*, 2009]. We expected hypocenter parameters to change in the 3D inversion and hence defined a depth range of 0.0 km to 30 km for the model volume with 60 grid points at 0.5 km spacing. Since FMTOMO automatically adds a cushion of boundary nodes, the total number of grid cells is (12 + 2) * (12 + 2) * (60 + 2) = 12,152. The refined grid has a theoretical maximum of (12 + 2) * 7 * (12 + 2) * 7 * (60 + 2) = 595,448 cells, if sources were present in each cell.

[18] Next, an initial velocity model was constructed by using a P wave minimum 1D-velocity model [*Lefeldt et al.*, 2009] hanging from the seafloor, constrained with multibeam bathymetry [*Ranero et al.*, 2003].

[19] When solving the forward problem, FMTOMO calculates the total travel time from source to receiver for events outside of the model volume (regional events) by embedding the model volume into the ak135 travel time tables [*Kennett et al.*, 1995]. However, the inversion process removes the mean of arrival time residuals, which leads to the use of relative arrival time residuals for regional sources throughout the inversion scheme. Relative arrivals time residuals do not constrain absolute velocities as the other two data sets, but they provide critical information to detect changes in the depth-velocity gradient. To constrain the depth of the base of the region of comparatively steep depth-velocity changes we have performed a series of squeeze tests described in detail below.

[20] We noticed that the ak135 travel time tables may not be appropriate for regional events with azimuthal direction approximately perpendicular to the trench axis, because their travel times are influenced by the fast slab. We solved the forward problem by embedding the P wave velocity model from *Syracuse et al.* [2008] into the ak135 model.

[21] A total of eight iterations of the tomographic inversion yielded a reduction of all-over RMS residuals from 196 ms to 174 ms, after which no improvement was obtained.

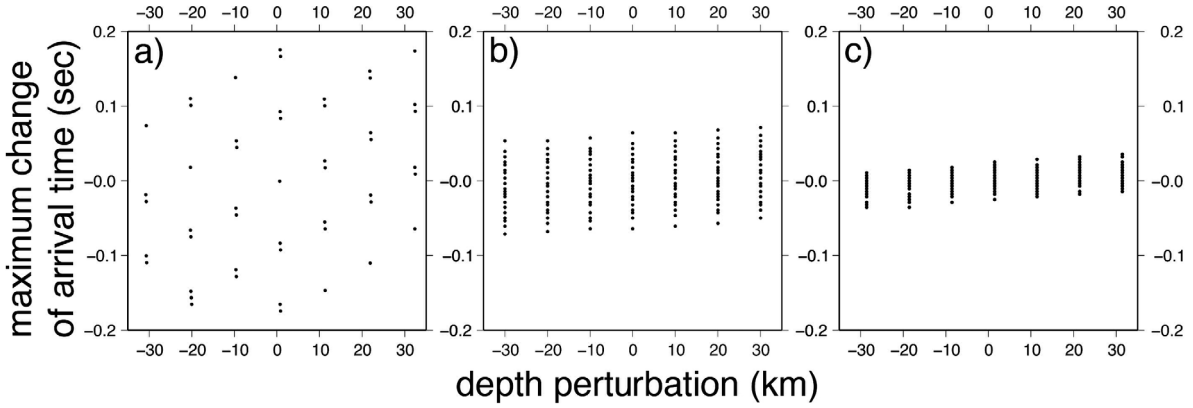


**Figure 2.** Results of a perturbation test for 3 (exemplary) events recorded in station obs31, and representative of regional seismicity. The *y* axis gives the maximum change of the arrival time in seconds and the *x* axis gives the perturbation of the depth. Each depth value has several values for the change of the arrival time. This is because for each depth value, numerous latitude and longitude values have been tested. Latitude and longitude have been perturbed between ±0.2° in 0.05° steps. Each event with a total arrival time change of ±0.1 s has been excluded, i.e., if the lowest value on the y-axes is less than −0.1 s or the highest value more than 0.1 s. (a) Perturbation test of a source with a focal depth of 50 km, a distance of 1.29°, and back azimuth of 48.54°. The maximum change is >±200 ms. The event was excluded. (b) Perturbation test of a source with a focal depth of 147 km, a distance of 2.22°, and back azimuth of 53.03°. The maximum change is <±100 ms. Again, the event was excluded. (c) Perturbation test of a source with a focal depth of 91 km, a distance of 6.64°, and back azimuth of 101.20°. The maximum change is < ± 35 ms and thus the event remained in the data set.

#### 3.2.1. Robustness of Arrival Times of Regional Sources

[22] The hypocenter of local earthquakes is re-calculated during the 3D tomography inversion process, but regional sources remain at their original locations.

[23] FMTOMO incorporates regional and teleseismic sources by using relative arrival times, which depend on hypocenter location and the global velocity model, but are not sensitive to relative changes of these parameters. E.g. a change of hypocenter location changes the ray parameter for a particular station, but the relative difference in ray parameter with two nearby stations will not change significantly, provided that the distance between those two stations is small compared to the distance to the source.

[24] To test the robustness of relative arrival times against changes in location of regional sources, we perturbed regional hypocenter parameters systematically in depth (±30 km), latitude and longitude (each ± 0.2°) to realistically account for large location uncertainties. We calculated arrival times of perturbed source locations, and the relative arrival times between stations. For each perturbation we calculated the maximum change of the relative arrival times within the network and excluded events with changes larger than ±100 ms (Figure 2). A total of 47 regional events past the analysis, that excluded all sources nearer than ∼250 km.

#### 3.2.2. Resolution and Error Estimation

[25] Accuracy of the calculation of velocity in grid cells in the model volume depends on both ray coverage and accurate travel time picks. The former is given by the active and passive source distribution, and the latter may be influenced by: (a) time errors during recording; (b) picking errors; (c) incorrect hypocenter location.

[26] Time errors might derive from inaccuracy of the recorder clocks. Clocks are set to GPS-time right before and right after deployment, and any deviation is assumed to be linear. This assumption was confirmed by the distribution of scattering of residuals, i.e., the difference between observed and calculated travel times through the final model obeys a normal distribution over time, and thus indicating that time errors are minimal. This analysis allows taking the standard deviation of the residuals as a measurement of the errors related to recording time, picking, and hypocenter uncertainty. For all stations, residuals and standard deviation are larger for microearthquakes, which are affected by all three types of errors, than for active seismic data affected only by time or picking errors (Table 1).

**Table 1.** Standard Deviation of the Residuals of All Sources (Local and Regional Seismicity, as Well as Wide-Angle Seismic Data) for Each OBH/S Station

| Station | Micro-earthquakes: Standard Deviation of Residual (ms) | Air Gun Shots: Standard Deviation of Residual (ms) | Regional Events: Standard Deviation of Residual (ms) |
|---|---|---|---|
| OBH 10 | 101 | 67 | 211 |
| OBH 11 | 156 | 78 | 167 |
| OBS 12 | 132 | 57 | 145 |
| OBH 13 | 149 | 81 | 239 |
| OBS 14 | 154 | 67 | 351 |
| OBH 16 | 121 | 92 | 275 |
| OBH 17 | 145 | 70 | 234 |
| OBS 18 | 98 | 59 | 148 |
| OBH 20 | 177 | 78 | 283 |
| OBH 21 | 163 | 84 | 213 |
| OBS 22 | 168 | 81 | 238 |
| OBH 23 | 223 | 93 | 380 |
| OBH 24 | 192 | 129 | 253 |
| OBH 25 | 157 | 63 | 212 |
| OBS 26 | 140 | 72 | 294 |
| OBH 27 | 158 | 69 | 349 |
| OBS 28 | 130 | 44 | 182 |
| OBS 29 | 172 | 83 | 390 |
| OBS 30 | 139 | 65 | 231 |
| OBS 31 | 203 | 82 | 303 |
| OBH 33 | 183 | 93 | 276 |

[27] Resolution and uncertainty of the velocity model were estimated with a combination of tests that include (I) velocity recovery tests; (II) 'Squeezing'' tests, and (III) input-model-dependency test.

#### 3.2.2.1. Velocity Recovery Tests

[28] Velocity recovery tests indicate where ray coverage has appropriate resolution to recover velocity layers in the upper ~14 km of the mantle. We used the P wave minimum 1D-velocity model [*Lefeldt et al.*, 2009] (Figure 3) and modified it to include reduced-velocity layers at different depths of the model. A forward calculation [*Rawlinson and Urvoy*, 2006] gave synthetic travel times for all sources of the data set. A Monte-Carlo distribution of errors was added to these travel times, which were then used as input travel times for an iterative inversion scheme that used the original P wave minimum 1D-velocity model [*Lefeldt et al.*, 2009] as starting model. Test results show that introduced layers can be reasonably well resolved to ~14 km below the Base of Crust (BOC) (Figure 4). However, when reduced-velocity layers are not fully recovered (Figures 4d and 4f), artificial high-velocities are generated beneath ~15 km below BOC. This artifact is an effect of sampling the deeper regions only with regional seismicity, which gives information on velocity gradients rather than absolute velocity.

#### 3.2.2.2. 'Squeezing' Tests

[29] 'Squeezing' tests were used to estimate the maximum depth a velocity anomaly may extend to satisfy the data set [e.g., *Allen and Tromp*, 2005]. Thereby, velocity anomalies are permitted only in a certain depth range, e.g., in the crust and 2 km below. Beneath, velocities are fixed to those of an 'unaltered' upper mantle ($V_p \geq 8.1$ km/s). This way, the velocity anomaly is 'squeezed' into a specific area during the iteration. The velocity model that is calculated in this way can be compared to the final 3D velocity model, in which reduced mantle velocities were allowed throughout all depths by comparing RMS, variance and chi-square ($|^2$) of both models. A significantly larger RMS, variance and $|^2$ in the 'squeezed' velocity model indicates that the area of reduced velocities must extend deeper into the mantle to satisfy the data set. Thus, this testing strategy can be used to constrain the 'deepest velocity anomaly' required by the data.

[30] Four models were tested with an iterative inversion scheme: A first test allowing velocity

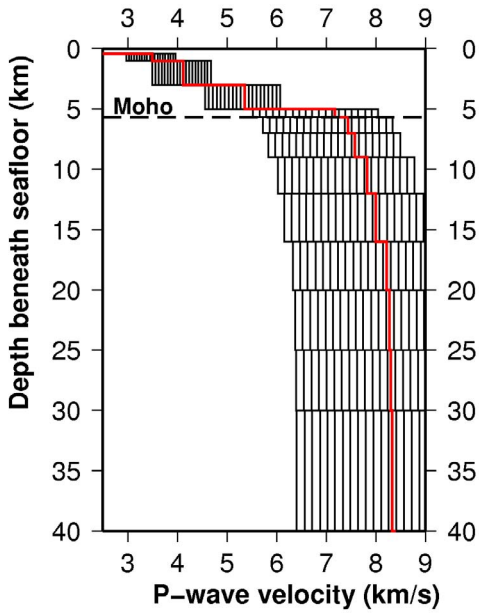


**Figure 3.** Range of velocity-depth profiles encompassing the 80 starting models used for the resolution test (black lines). For each starting model, the thickness of the layering remained the same, but velocity and gradients were altered randomly. The red line is P wave minimum 1D-velocity model after *Lefeldt et al.* [2009] for comparison.

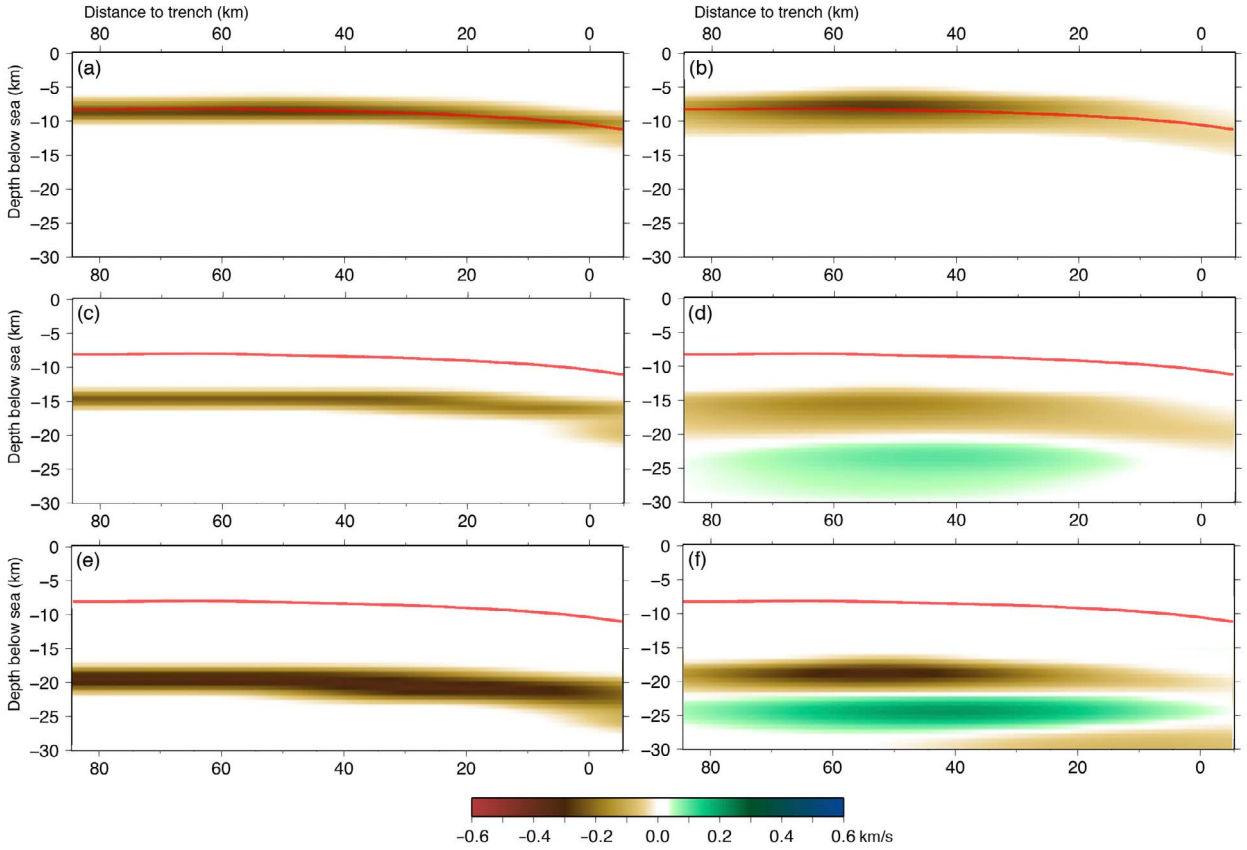


**Figure 4.** Resolution tests to determine the depth to which reduced-velocity anomalies from a starting model can be resolved with the experiment coverage. (a, c, and e) Synthetic velocity models with reduced-velocity layers at various depths were generated and synthetic travel times were determined using forward ray-tracing. Errors were added to the synthetic travel-times using a Monte-Carlo distribution. (b, d, and f) The recovered velocity models. Negative velocity values indicate reduced velocities. Red line marks Base of Crust (BOC). Synthetic model in Figure 4a introduces a reduced-velocity layer between −2.5 km and 2.5 km below BOC. The recovered model in Figure 4b indicates good resolution for this area. Synthetic model in Figure 4c introduces a reduced-velocity layer at 5 km to 8 km below BOC and recovered model in Figure 4d suggests good resolution as well, though the reduced-velocity layer is smeared between 5.5 km and 11 km below BOC, which is compensated by an artifact of a increased-velocity layer beneath. Synthetic model in Figure 4e introduces a reduced-velocity layer at 9 km to 14 km below BOC and inversion in Figure 4f recovers the model, but deeper velocities are overestimated.

changes only in crust (Figures 5a and 5b). In a second test, the uppermost 2 km of mantle were added to the area in which velocity changes were allowed (Figures 5c and 5d). A third (Figures 5e and 5f) and a forth test included the uppermost 6 and 10 km of mantle respectively (Figures 5g and 5h). Starting model for all tests was the P wave minimum 1D-velocity model. Results shown in Figure 5 suggest that a reduced-velocity anomaly with a depth-extension of >10 km below BOC is needed to satisfy the data set.

### 3.2.2.3. Statistical Velocity Uncertainty Analysis

[31] We evaluated the combined influence on the velocity model of both, errors in travel time picks and ray coverage. For this, we randomly created 80 different 1D-starting models that cover a wide range of possible P wave velocities (Figure 3), but with the boundary conditions that velocity increases with depths only; $V_p \geq 1.56$ km/s and $V_p = 6.5$–9 km/s in the lower layer (30 to 40 km below seafloor).

[32] For each of the 80 starting models, we iterated FMTOMO eight times using the original travel-time picks. Further, we added errors to the time picks for each station: For each input data set we defined the minimum-maximum errors after Table 1. And for each of the 80 starting models, we randomly added errors between these minimum-maximum values on all travel time picks using the Monte Carlo method.

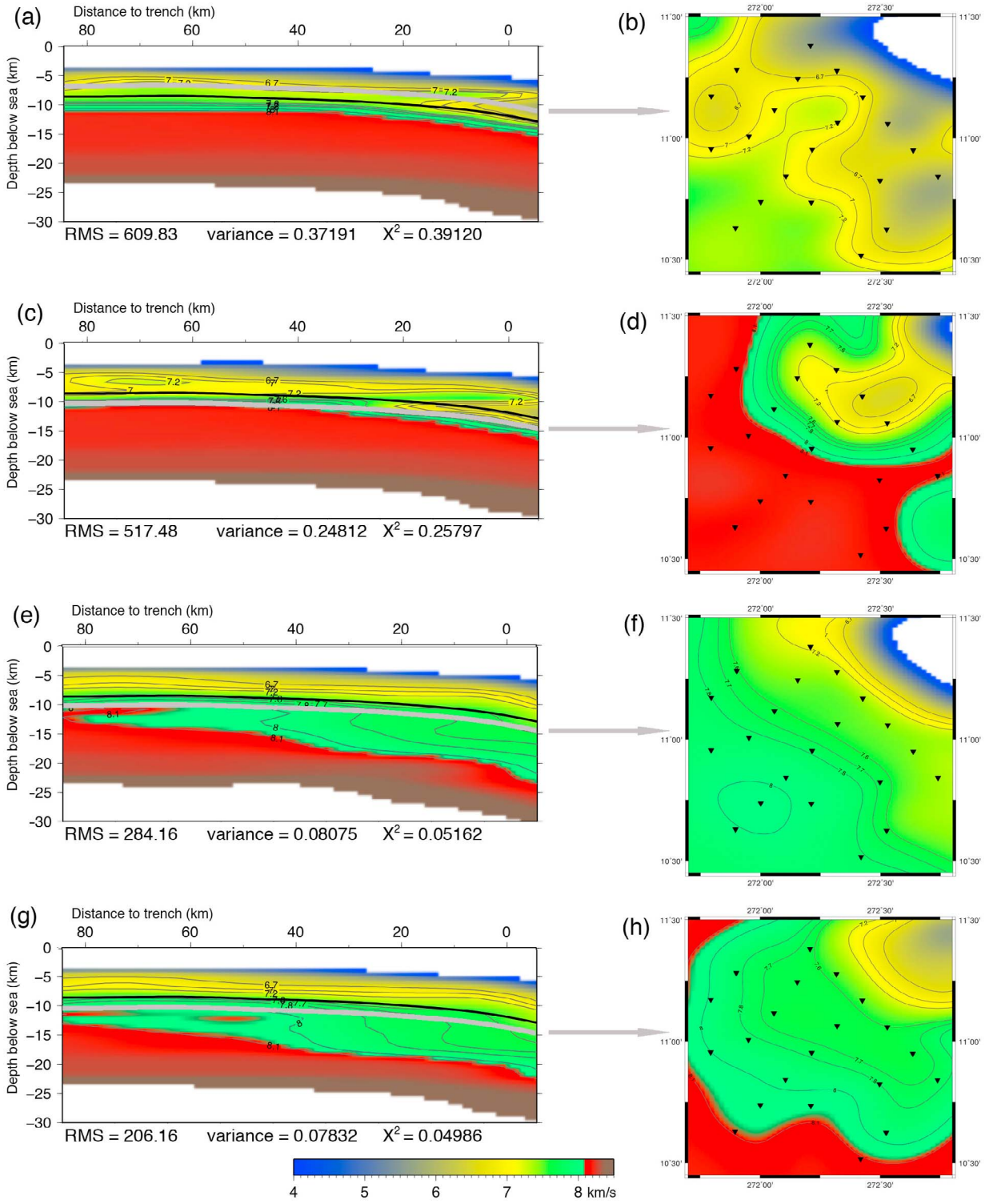
(a)
Distance to trench (km)
80 60 40 20 0
Depth below sea (km)
0 −5 −10 −15 −20 −25 −30
RMS = 609.83 variance = 0.37191 X² = 0.39120
(b)
272°00' 272°30'
11°30' 11°00' 10°30'
(c)
Distance to trench (km)
RMS = 517.48 variance = 0.24812 X² = 0.25797
(d)
(e)
Distance to trench (km)
RMS = 284.16 variance = 0.08075 X² = 0.05162
(f)
(g)
Distance to trench (km)
RMS = 206.16 variance = 0.07832 X² = 0.04986
(h)
4 5 6 7 8 km/s

**Figure 5**

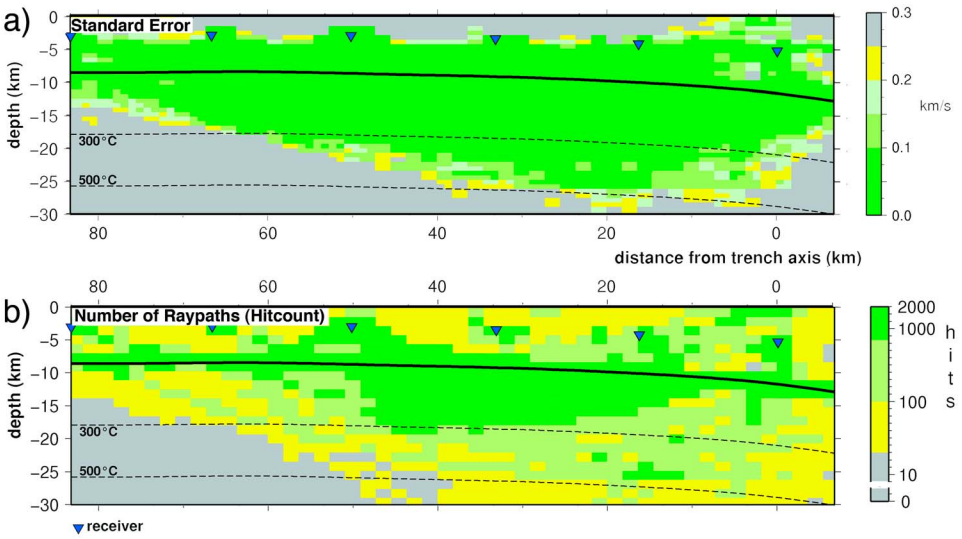


**Figure 6.** (a) Standard error and (b) raypath coverage (as hit counts) for the great circle cross section through the velocity model volume in Figure 9. The area with a standard error of >0.25 km/s has been masked.

[33] The final velocity models calculated from 80 different starting models with 80 different error distributions provides a statistically meaningful way to calculate the standard deviation for each grid cell, which yields the uncertainty in the velocity estimation [*Tarantola*, 1987].

[34] Figures 6 and 7 show standard error for cross sections and depth slices of final velocity model in Figures 9 and 10. Figures 6 and 8 show raypath coverage for the same cross section and depth slices. Standard error in most of the model used for the interpretation is below 0.1 km/s.

[35] The final 3D-velocity model used for interpretation (Figure 9 and 10) displays changes in depth, and gradient of the lower part of the low-velocity volume that vary with distance from the trench axis. The squeeze test show that near the trench axis, the absolute velocities of the deeper portions of the anomalous mantle are not as well constrained as the shallow portions, because the deeper region is only constrained by arrivals from regional earthquakes. However, the test also show that the steep gradients mapped in the anomalous-velocity region are gradually disappear in deeper mantle regions, thus placing constrains on the location of the bottom of the area of intense mantle velocity alteration, either by fracturing or more likely a combination of fracturing and mineral transformation.

## 4. Discussion

[36] The deeper region of anomalous low velocities has been illuminated with the local and regional seismicity. Velocity uncertainty of the 3D P wave velocity model shown in Figures 9 and 10 was constrained with squeezing tests, checkerboard resolution tests, and Monte Carlo inversion. Error bounds are sufficiently well constrained to reliably define the limits of the volume of anomalous mantle velocity. The velocity uncertainty tests indicate that the inversion constrains well the

**Figure 5.** Results of "squeezing" tests. (a) Cross section and (b) depth slice along gray line in Figure 5a through the final velocity model after eight iterations, with inversion restricted to crust. RMS, variance and $|^2$ are comparatively large (values are given below Figure 5a). (c) Cross section and (d) depth slice through final velocity model when inversion is restricted to crust and uppermost 2 km of mantle. RMS, variance and $|^2$ are comparatively large. The model contains velocities of >7.2 km/s in the crust and lower velocities beneath. (e) Cross section and (f) depth slice through final velocity model when inversion is restricted to crust and uppermost 6 km of mantle. The crust model is smooth and well-constrained, but the mantle shows high-velocity layers at 60 km to 80 km distance from the trench. RMS, variance and $|^2$ are comparatively large. (g) Cross section and (h) depth slice through final velocity model when inversion is restricted to crust and upper most 10 km of mantle. The model is generally comparable to Figures 9 and 10, although it contains high-velocity anomalies at 60 and 80 km distance from trench axis. RMS, variance and $|^2$ are larger than final model in Figures 9 and 10.

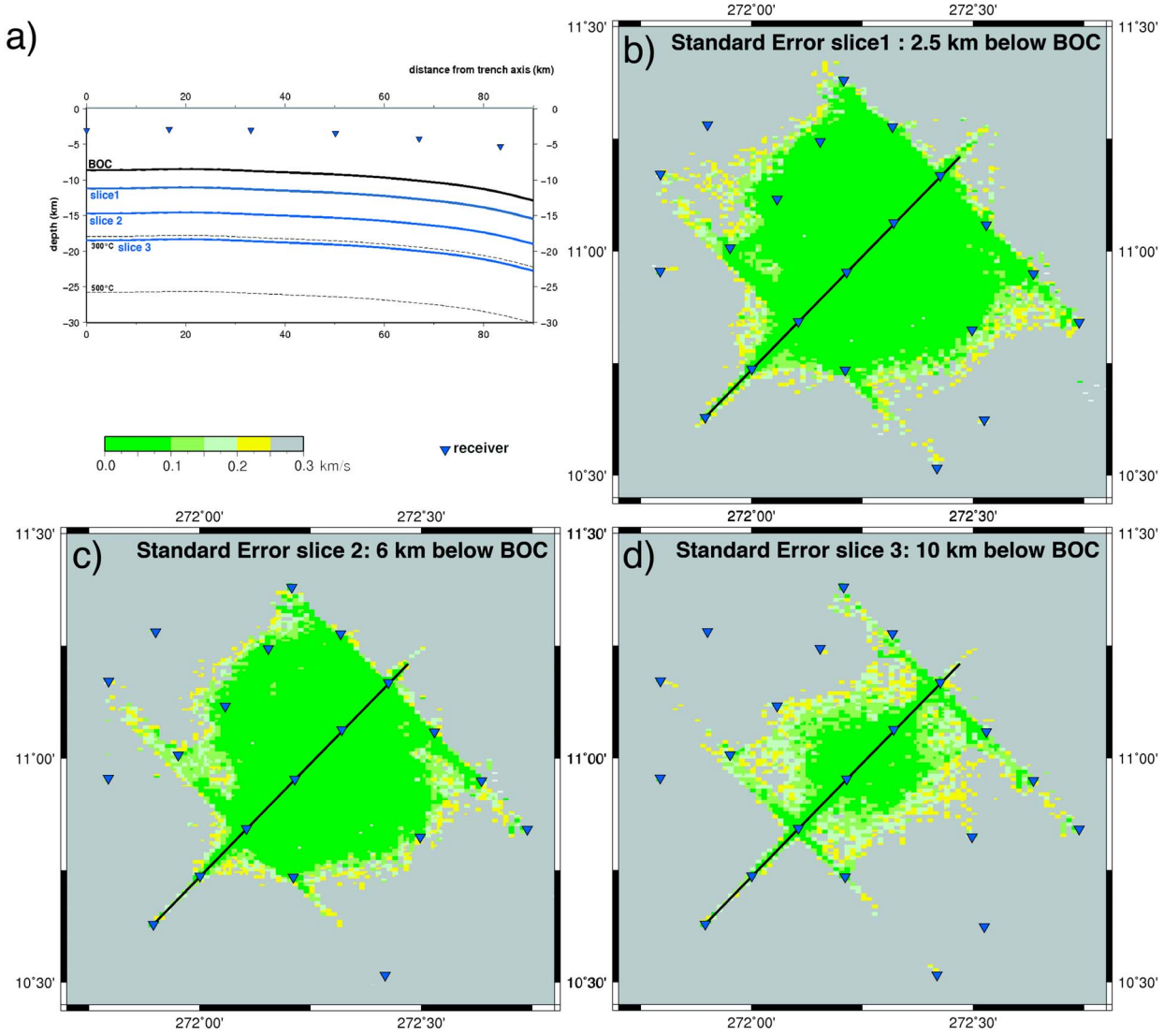


**Figure 7.** (a) Cross section showing location of slices. Each slice is at constant depth below the base of the crust (BOC). (b) Standard error of the 3D velocity model for depth slice of 2.5 km below BOC. (c) Standard error of the 3D velocity model for depth slice of 6 km below BOC. (d) Standard error of the 3D velocity model for depth slice of 10 km below BOC. Slices in Figures 7b–7d are equivalent to Figures 10b–10d. Areas with a standard error of >0.25 km/s (gray area) are masked in Figures 7b–7d.

location of the transition from a shallower, comparatively steeper velocity gradient with anomalously low values, to a deeper fairly constant depth-velocity profile with velocities indicating pristine mantle.

[37] Well-constrained velocities have been obtained across a volume 50 km wide perpendicular to the trench axis to 50–20 km wide parallel to the trench axis (Figure 10), to a depth of 12–25 km (Figure 9). The model extends 80 km perpendicular to the trench axis along one of the active-source profiles (Figure 9). Uppermost mantle velocity of the Cocos plate offshore Nicaragua away from the region of bending-related deformation ranges from 8.2 to 8.3 km/s [*Wilson et al.*, 2003]. Thus, the ~7.5 km/s mantle velocity mapped right under the BOC across the entire volume indicates altered mantle everywhere.

[38] The vertical cross section (Figure 9a), and slices of the velocity model taken at a constant depth below the BOC (2.5, 6, and 10 km distance from the BOC in Figure 10) show a gradual velocity reduction in the upper 10 km of the mantle approaching the trench axis. This velocity reduction

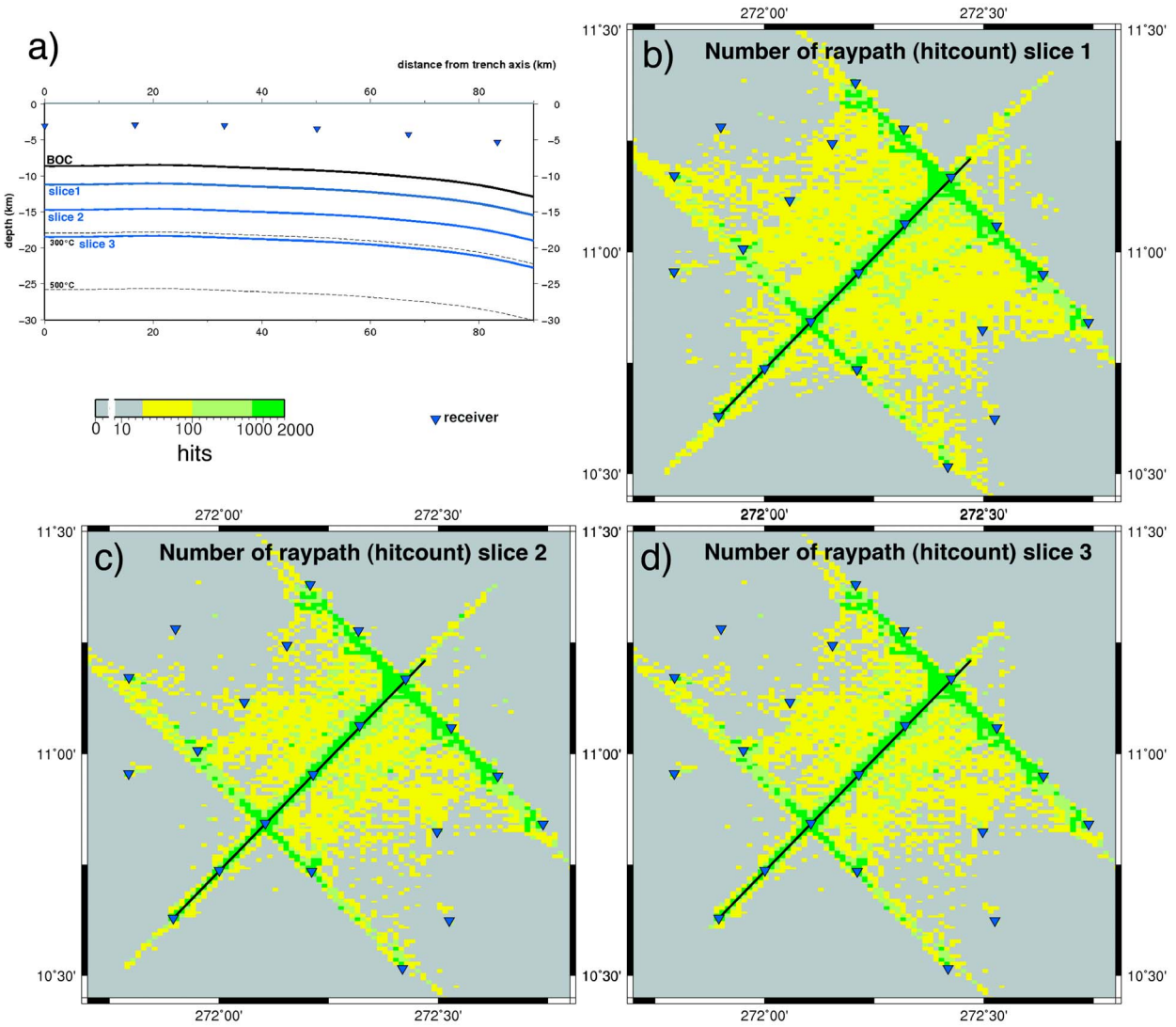


**Figure 8.** (a) Cross section showing location of slices. Each slice is at constant depth below the base of the crust (BOC). (b) Raypath coverage (hit counts) for depth of 2.5 km below BOC. (c) Raypath coverage (hit counts) for depth of 6 km below BOC. (d) Raypath coverage (hit counts) for depth of 10 km below BOC. Slices in Figures 8b–8d have a constant depth beneath the Base of Crust and are equivalent to Figures 10b–10d.

indicates growing mantle fracturing and possibly associated hydration as the plate travels across the trench region and is increasingly deformed. To investigate the volume of anomalous mantle, we compare depth-velocity functions of the model with pristine peridotite velocity at ~60, ~35 and ~10 km from the trench axis. The sites represent lithosphere at 0.76, 0.44 and 0.12 m.y. before subduction respectively, and differences in their velocity-depth function may be interpreted as caused by evolving mantle fracturing and associated hydration (Figures 9b–9d). At ~60 km site (Figure 9b), velocity corresponding to pristine peridotite occurs -within error bounds- at 6–9 km below the BOC. At ~35 and ~10 km sites (Figures 9c and 9d), velocity of pristine peridotite occurs at 9–10 km below the BOC for both locations. Similarly, depth slices display a laterally constant velocity for the data volume at 10 km below the BOC (Figure 10d) and velocity reduction toward the trench axis at shallower depths (Figures 10c and 10b). Therefore, fracturing/hydration detectable with our experiment appears restricted to ~10 km of mantle below the BOC.

[39] Although significant fracturing and associated water penetration may be restricted to the upper 10 km of mantle, velocity-depth functions differ

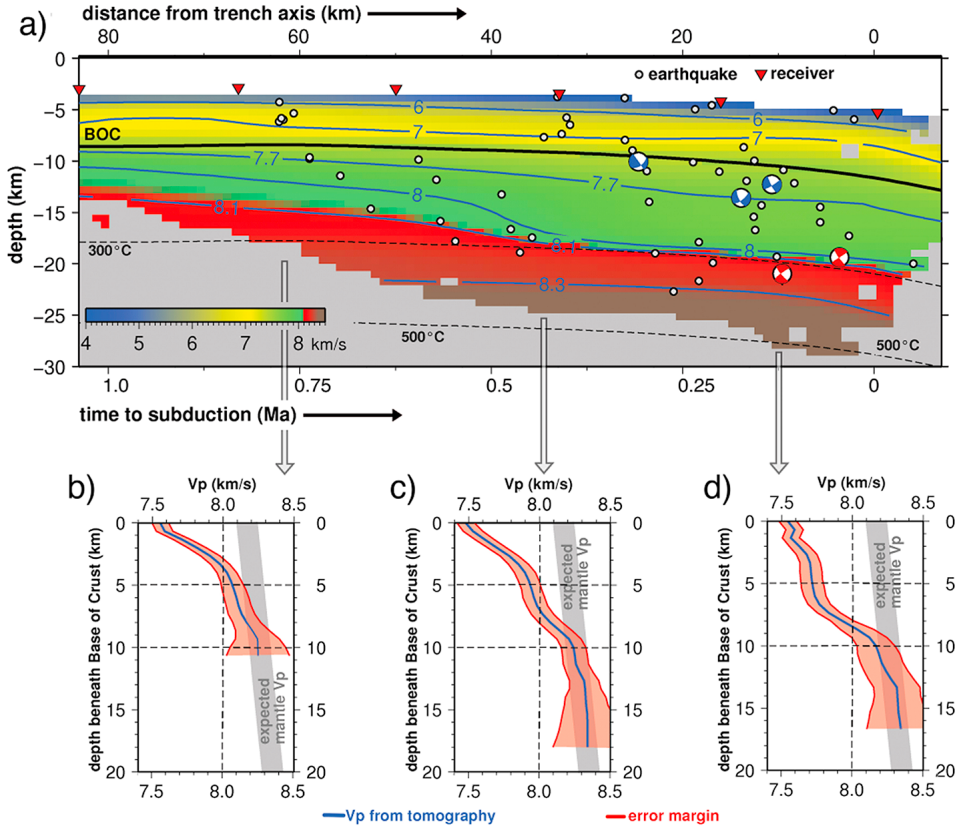


**Figure 9.** Velocity from 3D tomographic inversion. (a) Vertical cross section perpendicular to the trench axis and across 3D velocity model. (Location is shown in Figure 1, yellow line.) Grey areas are unconstrained. Velocities are color-coded so that yellow to green below the base of the crust (BOC) indicate partially serpentinized peridotite, reddish a transition from very slightly serpentinized to unaltered peridotite, and brown unaltered peridotite. White-filled black circles are projected micro-earthquakes, including focal mechanisms of 3 normal fault (blue) and 2 thrust fault (red) events. Thrusts occur where velocity indicate little mantle hydration. Black dashed lines are estimated 300°C and 500°C isotherms. Distance from the trench axis in upper axis is converted to time to subduction in lower axis with current convergence rate (80 km $Myr^{-1}$). The 1D velocity-depth functions at (b) 10, (c) 35, and (d) 60 km from model in Figure 9a. Reddish area is velocity error bounds. Grey bars bound expected P wave velocity for peridotite.

across the area indicating variable degrees of mantle alteration. Right below the BOC the velocity is ~7.5 km/s for all three sites, but deeper velocity gradients change (Figure 9). The ~60 km site (Figure 9b) has the steepest gradient, where velocities approach ~8 km/s at ~3 km below BOC and unaltered mantle at ~6 km. At the ~35 km site (Figure 9c), with a gentler gradient, velocities approach ~8 km/s at ~7 km below BOC and pristine mantle at ~9 km. The ~10 km site (Figure 9d) has an upper segment with the gentlest gradient, with velocities approaching ~7.7 km/s at ~7 km below BOC, followed by steep gradient to unaltered mantle velocities at ~10 km.

[40] We interpret the occurrence at all sites of a ~7.5 km/s velocity right below BOC as indicating an upper limit in the amount of alteration in this region. If the entire velocity reduction were caused by mineral hydration, it implies a ~15% of peridotite to serpentinite transformation. However, the velocity reduction may be due to the combined effect of fluid-filled fractures in fault zones and serpentinization. As the plate converges 25 km toward the trench axis (from ~60 to ~35 km site) deformation and water influx continue altering further the velocity of the upper ~5 km kilometers of mantle, as indicated by the comparatively gentler velocity gradient at ~35 km site (compare Figures 9b and 9c). Here, a velocity reduction between 5 to 10 km depth indicates that enhanced fracturing and water transport extend down up to 10 km below BOC. Another 25 km of convergence (from ~35 km to ~10 km site) does not deepen further the alteration front, although increased fracturing and associated mantle hydration have

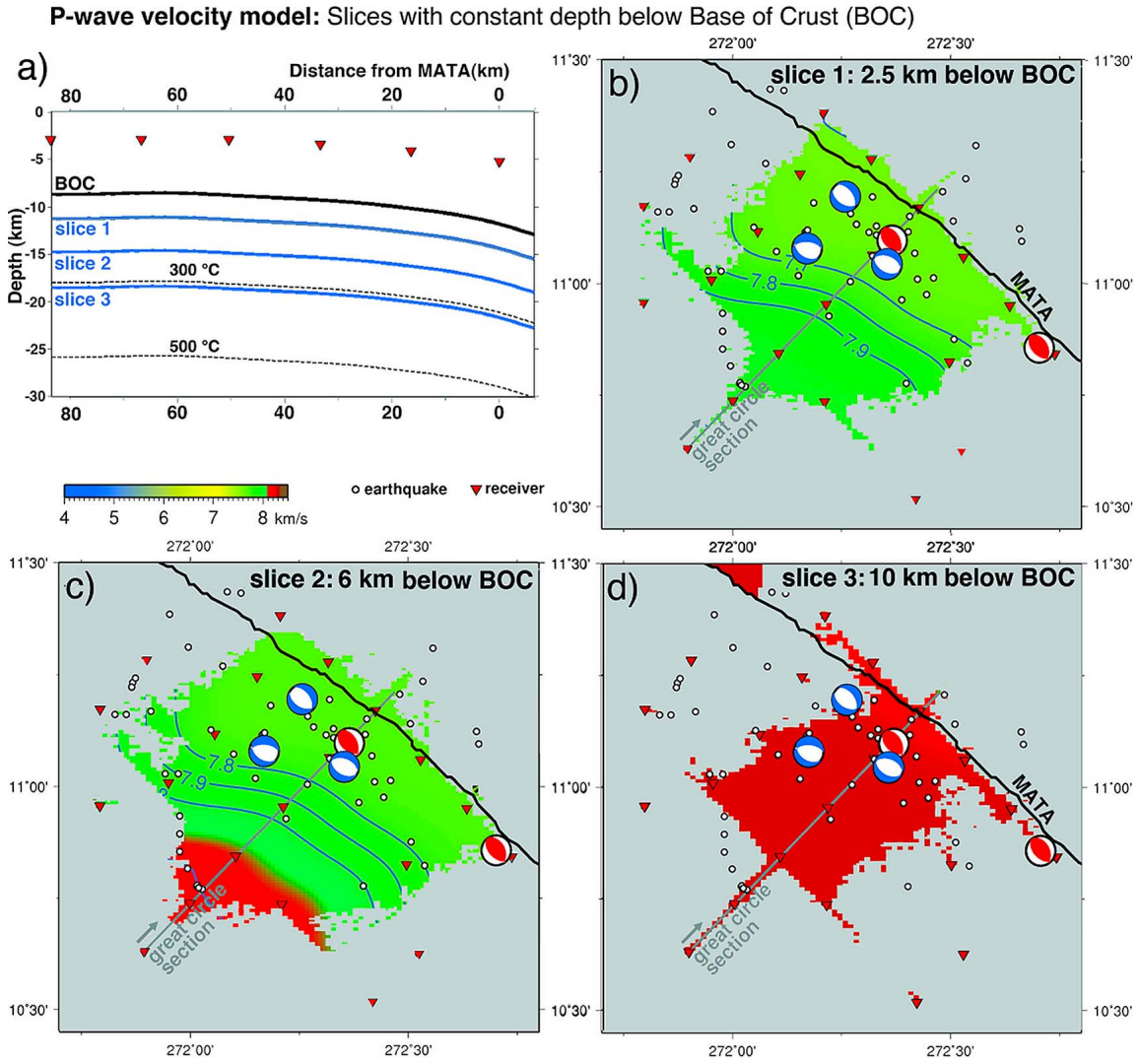


**Figure 10.** Depth slices across the P wave 3D velocity model. (a) Cross section showing location of slices, each slice is at constant depth below the base of the crust (BOC). (b) Depth slice at 2.5 km below BOC. (c) Depth slice at 6 km below BOC. (d) Depth slice at 10 km below BOC. Dark gray line in Figures 10b–10d marks location of vertical cross section in Figure 9a. White-filled black circles are micro-earthquake epicenters, including focal mechanisms of 3 normal fault (blue) and 2 thrust fault (red) events. Focal mechanisms are projected and did not necessarily occur at slice depth.

additionally reduced velocities in the 10 km below BOC (compare Figures 9c and 9d).

[41] Large intraplate, normal-fault earthquakes fracture deep into the mantle, what possibly leads to the creation of pathways for water to percolate and hydrate the mantle down to rupture depth [*Peacock*, 2001], or alteration might be limited by serpentine stability if it is shallower than rupture depth. Estimated hypocenter depth of the centroid of large teleseismic earthquakes in the region is 15–25 km ± 10–15 km depth below Moho [*Christensen and Ruff*, 1988; *Lefeldt and Grevemeyer*, 2008]. The rupture of those normal fault events propagates downdip several kilometers from their centroid depth. Thus, large teleseismic earthquakes cut considerably deeper than the base of the volume of anomalous velocity. This observation indicates that rupture depth of large earthquakes, although may create permeability, does not relate to the depth extend of mantle alteration.

[42] A likely requirement for the occurrence of significant mantle hydration is that fractures stay open, i.e., under tension, long enough to allow pervasive deep water circulation. The stress field of

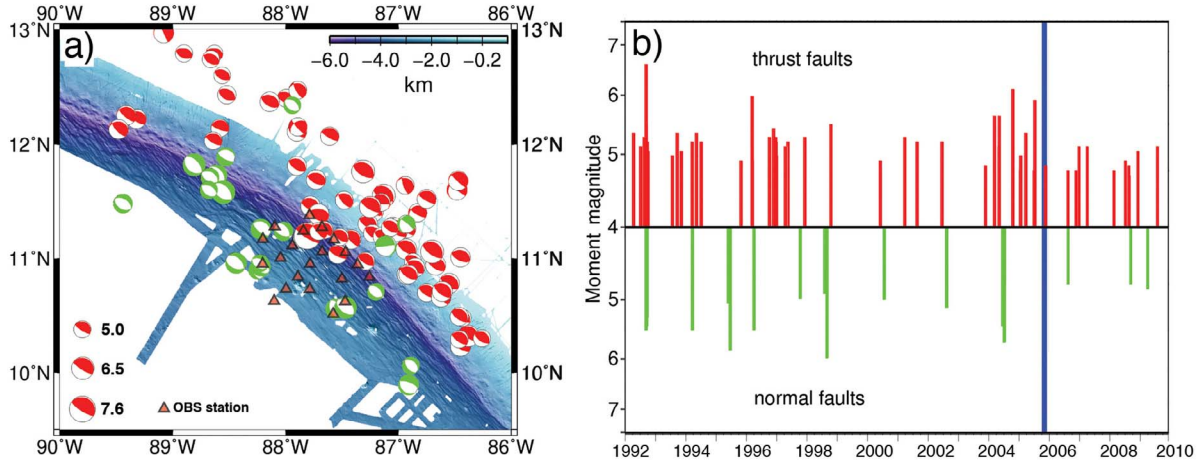


**Figure 11.** Teleseismic shallow earthquakes (<50 km depth) within the study area from the Global Centroid Moment Tensor (GCMT) catalog. (a) Focal mechanisms projected on a multibeam bathymetry map of the trench. Red mechanisms are interplate thrust and green mechanisms are intraplate normal faults. Red triangles show stations of the seismological network. (b) Time distribution of seismicity shown in Figure 11a. Red bars are interplate thrust events and green bars trench-outer rise normal fault events. Blue bar marks the deployment period of the seismic network at the trench.

the ocean plate in the outer rise region is sensitive to the state of coupling of the overriding and under-thrusting plates at the interface of the subduction zone. The ocean plate in the outer rise might show different response times if inter-plate coupling changes, depending on whether the strain migration to the outer rise is of dynamic, static, or visco-elastic nature [*Ammon et al.*, 2008; *Lefeldt and Grevemeyer*, 2008]. Large normal-fault earthquakes are possibly related to slab-pull stresses that reach the outer rise region only when overriding and under-thrusting plates are partially uncoupled typically after inter-plate thrust events [*Ammon et al.*, 2008]. The trench-outer rise region offshore Nicaragua has teleseismic normal-fault events about once a year, rupturing one of the 50–100 normal faults visible in bathymetry), so that each normal fault might rupture in a >∼4.5 Mw event every 50–100 years (Figure 11). This rupture interval seems too infrequent to promote important fracturing and plate hydration.

[43] The depth of serpentine stability might potentially control the depth of hydration [*Carlson and Miller*, 2003]. At the pressures encountered in the incoming oceanic lithosphere, serpentine minerals are stable to 500°C–600°C [*Ulmer and Trommsdorff*, 1995]. The estimated thermal structure of the plate using *McKenzie et al.* [2005] indicates that the 500°C isotherm occurs at ∼17 km below the BOC. When comparing velocity to temperature shows that the 500°C isotherm is considerably deeper than the base of the anomalous mantle velocity located 10 km below the BOC (Figure 9a). In the calculation the temperature estimation is simplified because it does not consider the competing effects of cooling by water penetration (that would move isotherms deeper) and exothermic heat release from serpentinization. However, the considerable depth difference between the alteration front, inferred from anomalously low velocity, and the 500°C isotherm, supports that depth limit of hydration in the region is not controlled by temperature.

[44] Focal mechanisms of micro-earthquakes recorded in the network provide information on the depth distribution of local stresses during the deployment period, which was 1.5 years after the last large normal fault event in the area and 0.75 years before the subsequent one (Figure 11), and thus it probably represent the "regular" stress state of the outer rise region between state that follows large inter-plate thrust events. Focal mechanisms, which could be determined for five micro-earthquakes [*Lefeldt et al.*, 2009], indicate the relationship between local stresses and mantle structure when they are projected on a cross section of the velocity model (Figure 9a). Two thrust-fault ruptures occurred at about 10 km below the BOC, i.e., at about the lower depth limit of anomalously low velocity. In contrast, normal fault mechanisms occurred at shallower depth where low velocities

and a steep gradient indicate mantle alteration. We assume that the regular state of stress of the incoming lithosphere at the trench – outer rise region is that of the inter-plate inter-seismic part of the seismic cycle, when coupling is comparatively stronger. Bending a thin ideally elastic-perfectly plastic plate [*Chapple and Forsyth*, 1979] would cause a transition from a tensional regime at top of the plate to a compressional stresses underneath. The transition in the Cocos Plate is marked by the change from normal-fault to thrust-fault focal mechanism with depth. Thus, the depth of significant mantle alteration detected in our experiment appears to be controlled by the depth of extensional deformation by plate bending.

[45] Although tensile cracks can be opened by fluid hydrofracturing even in a compressive setting [*Sibson et al.*, 1988], fluid percolation transport is controlled by fluid pressure gradient according to Darcy's law. At upper mantle depth, fluid pressure is strongly related to solid pressure [*Faccenda et al.*, 2009], so that fluid will not penetrate the area characterized by compression and over-pressure.

[46] During the two months deployment the network recorded ~90 micro-earthquakes within a trench area about 120 x 80 km in dimensions (Figure 1). Multibeam bathymetry shows large trench-parallel faults that can be followed for 50–80 km, and are spaced every 2–3 km [*Peacock*, 2001]. Thus, the observed average seismicity of 1.5 events per day in the network area with 40–100 large, visible faults, indicates that each large fault – or a segment of them - ruptures every 1–2 months in average. Such frequent bending-related deformation possibly maintains fractures in fault zones regularly open and modulates fluid percolation into the plate.

## 5. Conclusions

[47] We have mapped in 3 dimensions and for the first time the volume of anomalously low mantle velocity of an oceanic plate at the trench. An error and uncertainty analysis has provided realistic constrains of the depth extent of anomalous mantle velocities.

[48] The depth extent of anomalous velocities is interpreted as the depth of alteration of the mantle by hydration, even though some reduction in velocity may be caused by fluid-filled open cracks of the bending-related faults that occur every 1–3 km across the trench slope.

[49] The depth correspondence of micro-earthquakes with normal fault mechanism and anomalous mantle velocity is interpreted to indicate that significant water penetration into the mantle at subduction trenches is controlled by bending stresses generating normal faulting that rupture, dilate and possibly permit water percolation on a monthly basis. Most large magnitude, deeper earthquakes on these same faults probably results from a deepening of the neutral plane by increased slab pull, but those events are about one order of magnitude less frequent and do not appear to contribute to significant water influx or fracturing that could unambiguously be detected with our experiment.

[50] Last, an upper limit for the water content in the oceanic plate offshore Nicaragua can be estimated by assuming that all the alteration detected with seismic methods is caused by mantle serpentinization, and that fracture effect on velocity at mantle depths is negligible: Using the formula by *Carlson and Miller* [2003], the average velocity for the upper 10 km of the mantle (Figure 9a) gives a serpentinization of ~10% or 1.2 wt% chemically bound water. This is equivalent to a water column of 375 m that is subducted in the upper mantle alone.

## Acknowledgments

[51] This publication is contribution 242 of the Sonderforschungsbereich 574 "Volatiles and Fluids in Subduction Zones" at Kiel University. We would like to thank Manuele Faccenda and one anonymous reviewer for their very useful and constructive comments and indications. The data presented in this study was collected during R/V Meteor cruises M66/3 and M66/4. We thank scientific participants and crews for their effort. The cruises were founded by DFG.

## References

Abers, G. A., T. Plank, and B. R. Hacker (2003), The wet Nicaraguan slab, *Geophys. Res. Lett.*, *30*(2), 1098, doi:10.1029/2002GL015649.

Allen, R. M., and J. Tromp (2005), Resolution of regional seismic models: Squeezing the Iceland anomaly, *Geophys. J. Int.*, *161*, 373–386, doi:10.1111/j.1365-246X.2005.02600.x.

Ammon, C. J., H. Kanamori, and T. Lay (2008), A great earthquake doublet and seismic stress transfer cycle in the central Kuril islands, *Nature*, *451*, 561–565, doi:10.1038/nature06521.

Barckhausen, U., C. R. Ranero, R. von Huene, S. C. Cande, and H. A. Roeser (2001), Revised tectonic boundaries in the Cocos Plate off Costa Rica: Implications for the segmentation of the convergent margin and for plate tectonic models, *J. Geophys. Res.*, *106*(B9), 19,207–19,220, doi:10.1029/2001JB000238.

Carlson, R. L., and D. J. Miller (2003), Mantle wedge water contents estimated from seismic velocities in partially serpentinized peridotites, *Geophys. Res. Lett.*, *30*(5), 1250, doi:10.1029/2002GL016600.

Chapple, W. M., and D. W. Forsyth (1979), Earthquakes and bending plates at trenches, *J. Geophys. Res.*, *84*, 6729–6749, doi:10.1029/JB084iB12p06729.

Christensen, D. H., and L. Ruff (1988), Seismic coupling and outer rise earthquakes, *J. Geophys. Res.*, *93*, 13,421–13,444, doi:10.1029/JB093iB11p13421.

Contreras-Reyes, E., I. Grevemeyer, E. R. Flueh, M. Scherwath, and M. Heesemann (2007), Alteration of the subducting oceanic lithosphere at the southern central Chile trench–outer rise, *Geochem. Geophys. Geosyst.*, *8*, Q07003, doi:10.1029/2007GC001632.

DeMets, C. (2001), A new estimate for present-day Cocos-Caribbean Plate motion: Implications for slip along the Central American Volcanic Arc, *Geophys. Res. Lett.*, *28*(21), 4043–4046, doi:10.1029/2001GL013518.

Faccenda, M., T. V. Taras, and L. Burlini (2009), Deep slab hydration induced by bending-related variations in tectonic pressure, *Nat. Geosci.*, *2*, 790–793, doi:10.1038/ngeo656.

Grevemeyer, I., N. Kaul, J. L. Diaz-Naveas, H. W. Villinger, C. R. Ranero, and C. Reichert (2005), Heat flow and bending-related faulting at subduction trenches: Case studies offshore of Nicaragua and central Chile, *Earth Planet. Sci. Lett.*, *236*(1–2), 238–248, doi:10.1016/j.epsl.2005.04.048.

Grevemeyer, I., C. R. Ranero, E. R. Flueh, D. Klaeschen, and J. Bialas (2007), Passive and active seismological study of bending-related faulting and mantle serpentinization at the Middle America trench, *Earth Planet. Sci. Lett.*, *258*, 528–542, doi:10.1016/j.epsl.2007.04.013.

Ivandic, M., I. Grevemeyer, A. Berhorst, E. R. Flueh, and K. McIntosh (2008), Impact of bending related faulting on the seismic properties of the incoming oceanic plate offshore of Nicaragua, *J. Geophys. Res.*, *113*, B05410, doi:10.1029/2007JB005291.

Ivandic, M., I. Grevemeyer, J. Bialas, and C. J. Petersen (2010), Serpentinization in the trench-outer rise region offshore of Nicaragua: Constraints from seismic refraction and wide-angle data, *Geophys. J. Int.*, *180*(4), 1253–1264, doi:10.1111/j.1365-246X.2009.04474.x.

Jarrad, R. D. (2003), Subduction fluxes of water, carbon dioxide, chlorine, and potassium, *Geochem. Geophys. Geosyst.*, *4*(5), 8905, doi:10.1029/2002GC000392.

Kennett, B. L. N., E. R. Engdahl, and R. Buland (1995), Constraints on seismic velocities in the Earth from travel times, *Geophys. J. Int.*, *122*, 108–124, doi:10.1111/j.1365-246X.1995.tb03540.x.

Kobayashi, K., M. Nakanishi, K. Tamaki, and Y. Ogawa (1998), Outer slope faulting associated with western Kuril and Japan trenches, *Geophys. J. Int.*, *134*, 356–372, doi:10.1046/j.1365-246x.1998.00569.x.

Lefeldt, M., and I. Grevemeyer (2008), Centroid depth and mechanism of trench-outer rise earthquakes, *Geophys. J. Int.*, *172*, 240–251, doi:10.1111/j.1365-246X.2007.03616.x.

Lefeldt, M., I. Grevemeyer, J. Gossler, and J. Bialas (2009), Intraplate seismicity and related mantle hydration at the Nicaraguan trench outer rise, *Geophys. J. Int.*, *178*, 742–752, doi:10.1111/j.1365-246X.2009.04167.x.

Masson, D. G. (1991), Fault patterns at outer trench walls, *Mar. Geophys. Res.*, *13*, 209–225, doi:10.1007/BF00369150.

McKenzie, D., J. Jackson, and K. Priestley (2005), Thermal structure of oceanic and continental lithosphere, *Earth Planet. Sci. Lett.*, *233*, 337–349, doi:10.1016/j.epsl.2005.02.005.

Meade, C., and R. Jeanloz (1991), Deep focused earthquakes and recycling of water into the Earth's mantle, *Science*, *252*, 68–72, doi:10.1126/science.252.5002.68.

Peacock, S. (2001), Are the lower planes of double seismic zones caused by serpentine dehydration in subducting oceanic mantle?, *Geology*, *29*, 299–302, doi:10.1130/0091-7613(2001)029<0299:ATLPOD>2.0.CO;2.

Peacock, S. M. (2004), Insight into the hydrogeology and alteration of oceanic lithosphere based on subduction zones and arc volcanisms, in *Hydrogeology of Oceanic Lithosphere*, edited by E. E. Davis and H. Elderfield, pp. 659–676, Cambridge Univ. Press, Cambridge, U. K.

Raleigh, C. B., and M. S. Paterson (1965), Experimental deformation of serpentinite and its tectonic implications, *J. Geophys. Res.*, *70*, 3965–3985, doi:10.1029/JZ070i016p03965.

Ranero, C. R., and V. Sallares (2004), Geophysical evidence for hydration of the crust and mantle of the Nasca Plate during bending at the north Chile trench, *Geology*, *32*(7), 549–552, doi:10.1130/G20379.1.

Ranero, C. R., J. Phipps Morgan, K. McIntosh, and C. Reichert (2003), Bending-related faulting and mantle serpentinization at the Middle America Trench, *Nature*, *425*, 367–373, doi:10.1038/nature01961.

Ranero, C. R., A. Villaseñor, J. Phipps Morgan, and W. Weinrebe (2005), Relationship between bend-faulting at trenches and intermediate-depth seismicity, *Geochem. Geophys. Geosyst.*, *6*, Q12002, doi:10.1029/2005GC000997.

Rawlinson, N., and M. Urvoy (2006), Simultaneous inversion of active and passive source datasets for 3-D seismic structure with application to Tasmania, *Geophys. Res. Lett.*, *33*, L24313, doi:10.1029/2006GL028105.

Rawlinson, N., M. de Kool, and M. Sambridge (2006), Seismic wavefront tracking in 3-D heterogeneous media: Applications with multiple data classes, *Explor. Geophys.*, *37*, 322–330, doi:10.1071/EG06322.

Rüpke, L. H., J. Phipps Morgan, M. Hort, and J. A. D. Connolly (2004), Serpentine and the subduction zone water cycle, *Earth Planet. Sci. Lett.*, *223*, 17–34, doi:10.1016/j.epsl.2004.04.018.

Seno, T., and D. G. Gonzalez (1987), Faulting caused by earthquakes beneath the outer slope of the Japan Trench, *J. Phys. Earth*, *35*, 381–407, doi:10.4294/jpe1952.35.381.

Seno, T., and Y. Yamanaka (1996), Double seismic zones, compressional deep trench-outer rise events and superplumes, in *Subduction: Top to Bottom*, *Geophys. Monogr. Ser.*, vol. 96, edited by G. E. Bebout et al., pp. 347–355, AGU, Washington, D. C.

Sibson, R. H., F. Robert, and K. H. Poulsen (1988), High-angle reserve faults, fluid-pressure cycling, and mesothermal gold-quartz deposits, *Geology*, *16*(6), 551–555, doi:10.1130/0091-7613(1988)016<0551:HARFFP>2.3.CO;2.

Staudigel, H., T. Plank, B. White, and H. U. Schmincke (1996), Geochemical fluxes during seafloor alteration of the basaltic upper oceanic Crust: DSDP sites 417 and 418, in *Subduction Top to Bottom*, *Geophys. Monogr. Ser.*, vol. 96, edited by E. Bebout et al., pp. 19–38, AGU, Washington, D. C., doi:10.1029/GM096p0019.

Syracuse, E. M., G. A. Abers, K. Fischer, L. MacKenzie, C. Rychert, M. Protti, V. González, and W. Strauch (2008), Seismic tomography and earthquake locations in the Nicaraguan and Costa Rican upper mantle, *Geochem. Geophys. Geosyst.*, *9*, Q07S08, doi:10.1029/2008GC001963.

Tarantola, A. (1987), *Inverse Problem Theory: Methods for Data Fitting and Model Parameter Estimation*, 613 pp., Elsevier, New York.

Ulmer, P., and V. Trommsdorff (1995), Serpentine stability to mantle depths and subduction-related magmatism, *Science*, *268*, 858–861, doi:10.1126/science.268.5212.858.

van Avendonk, H. J. A., W. S. Holbrook, D. Lizarralde, and P. Denyer (2011), Structure and serpentinization of the subducting Cocos plate offshore Nicaragua and Costa Rica, *Geochem. Geophys. Geosyst.*, *12*, Q06009, doi:10.1029/2011GC003592.

Wilson, D. S., et al. (2003), Leg 206 summary, *Proc. Ocean Drill. Program Initial Rep.*, *206*, 1–117.